

Constraining the mass and redshift evolution of the hydrostatic mass bias using the gas mass fraction in galaxy clusters

R. Wicker¹, M. Douspis¹, L. Salvati¹, N. Aghanim¹

Université Paris-Saclay, CNRS, Institut d’Astrophysique Spatiale, 91405, Orsay, France
e-mail: raphael.wicker@ias.u-psud.fr

Received XXX; accepted XXX

ABSTRACT

The gas mass fraction in galaxy clusters is a convenient probe to use in cosmological studies, as it can help derive constraints on a collection of cosmological parameters. It is however subject to various effects from the baryonic physics inside galaxy clusters, which may bias the obtained cosmological constraints. Among different aspects of the baryonic physics, in this paper we focus on the impact of the hydrostatic equilibrium assumption. We analyse the hydrostatic mass bias B , constraining a possible mass and redshift evolution of this quantity and its impact on the cosmological constraints. To that end we consider cluster observations of the *Planck*-ESZ sample and evaluate the gas mass fraction using X-ray counterpart observations. We show a degeneracy between the redshift dependence of the bias and cosmological parameters. In particular we find a 3.8σ evidence for a redshift dependence of the bias when assuming a *Planck* prior on Ω_m . On the other hand, assuming a constant mass bias would lead to the extreme large value of $\Omega_m > 0.849$. We however show that our results are entirely dependent on the cluster sample we consider. In particular, the mass and redshift trends that we find for the lowest mass-redshift and highest mass-redshift clusters of our sample are not compatible. Nevertheless, in all the analyses we find a value for the amplitude of the bias that is consistent with $B \sim 0.8$, as expected from hydrodynamical simulations and local measurements, but still in tension with the low value of $B \sim 0.6$ derived from the combination of cosmic microwave background primary anisotropies with cluster number counts.

Key words. Cosmology: large-scale structure of Universe – Cosmology: Cosmological parameters – Galaxies: clusters: general – Galaxies: clusters: intracluster medium – X-rays: galaxies: clusters – Methods: data analysis

1. Introduction

Galaxy clusters are the most massive gravitationally bound systems of our universe, and as such they contain a wealth of cosmological and astrophysical information. They can be used either as powerful cosmological probes (White et al. (1993), Allen et al. (2011)) or as astrophysical objects of study, to better characterise the physics of the intra-cluster medium (ICM, Sarazin (1988)) and how these structures are connected to the rest of the cosmic web. Constraints on the matter density Ω_m or the amplitude of the matter power spectrum σ_8 can be inferred from several galaxy cluster observables. One can for instance use cluster number counts, their clustering, or the properties of their gas content to constrain cosmological parameters (see e.g. Kravtsov & Borgani (2012) or Allen et al. (2011) for reviews). Among the more recent probes, one can also cite the cluster sparsity (Balmès et al. 2013).

The baryon budget of these objects is also interesting in the aspect of galaxy clusters as cosmological probes, and especially the hot gas of the ICM which is composing the major part of the baryonic matter inside clusters. Indeed the gas mass fraction of galaxy clusters, f_{gas} , is considered to be a good proxy for the universal baryon fraction (Borgani & Kravtsov 2011), and can be used to constrain cosmological parameters including the matter density Ω_m , the Hubble parameter h , the Dark Energy density Ω_{DE} or the Equation of State of Dark Energy w (see e.g. Allen et al. (2008), Holanda et al. (2020), Mantz et al. (2022) and references therein).

The gas content inside galaxy clusters is however also affected by baryonic physics. Such baryonic effects need to be taken into account while performing the cosmological analysis, as they introduce systematic uncertainties in the final constraints (see e.g. the discussions from McCarthy et al. (2003a), McCarthy et al. (2003b), Poole et al. (2007), Hoekstra et al. (2012), Mahdavi et al. (2013), Ruan et al. (2013), Sakr et al. (2018)).

For instance, feedback mechanisms inside clusters, like Active Galactic Nuclei (AGN) heating, can drive gas out of the potential wells, resulting in slightly gas-depleted clusters. This depletion of galaxy clusters’ gas with respect to the universal baryon fraction is accounted for by the depletion factor Υ (Eke et al. (1998), Crain et al. (2007)). This depletion factor has been thoroughly studied in hydrodynamical simulations throughout the years, in clusters (Kravtsov et al. (2005), Planck et al. (2013), Sembolini et al. (2016), Henden et al. (2020), and references therein) as well as in filaments (Galárraga-Espinosa et al. 2021). As a result, this parameter can be very well constrained and robustly predicted in numerical simulations. Secondly, galaxy clusters are often assumed to be in hydrostatic equilibrium (HE hereafter). Nevertheless, non-thermal processes such as turbulence, bulk motions, magnetic fields or cosmic rays (Lau et al. (2009), Vazza et al. (2009), Battaglia et al. (2012), Nelson et al. (2014), Shi et al. (2015), Biffi et al. (2016)), might cause a departure from the equilibrium condition in the ICM. Therefore, the HE assumption leads to cluster mass estimations biased towards lower values with respect to the total cluster mass. The impact of non-thermal processes, and therefore an evaluation for the bias in the cluster mass estimation, was first

considered in hydrodynamical simulations (Rasia et al. 2006). Since then, a parametrization for this mass bias has been introduced also in observations, for instance when detecting clusters in X-ray or millimeter wavelengths, the latter exploiting the thermal Sunyaev-Zeldovich effect (Sunyaev & Zeldovich 1972) (tSZ hereafter) (see Pratt et al. (2019) for a review). We stress that this bias affects all the observables which might assume hydrostatic equilibrium when evaluating cluster masses, and thus the gas mass fraction. Throughout the paper we define this mass bias as $B = M_{HE}/M_{tot}$.

If the depletion factor is well constrained and understood, this is not the case for the hydrostatic mass bias as its value is still debated. In a number of analysis including weak lensing works (WtG (von der Linden et al. 2014), CCCP (Hoekstra et al. 2015), Okabe & Smith (2016), Sereno et al. (2017)), tSZ number counts (Salvati et al. 2019), X-ray observations (Eckert et al. 2019) or hydrodynamical simulations (McCarthy et al. (2017), Bennett & Sijacki (2021)), this mass bias is estimated to be around $B \sim 0.8 - 0.85$. The works from Planck Collaboration et al. (2014), Planck Collaboration et al. (2016) however show that to alleviate the tension on the amplitude of the matter power spectrum σ_8 between local and cosmic microwave background (CMB hereafter) measurements, a much lower B is needed. Indeed when combining CMB primary anisotropies and tSZ cluster counts, CMB measurements drive the constraining power on the cosmological parameters and thus on the bias, favoring a bias $B \sim 0.6 - 0.65$. This result was confirmed later on by Salvati et al. (2018) and Planck Collaboration et al. (2020). In addition, the study from Salvati et al. (2018) shows that when forcing $B = 0.8$ while assuming a *Planck* cosmology, the observed cluster number counts are way below the number counts predicted using the CMB best-fit cosmological parameters. In other words, when assuming $B = 0.8$ with a CMB cosmology, one predicts approximately thrice as many clusters as what is actually observed.

As the precise value of the mass bias is still an open matter and has a direct impact on the accuracy and precision of the cosmological constraints deduced from galaxy clusters, we propose a new and independent measurement of this quantity. In this paper we use the gas mass fractions of 120 galaxy clusters from the *Planck*-ESZ sample Planck Collaboration et al. (2011) to bring robust constraints on the value of the hydrostatic bias. More importantly, we aim at studying the potentiality of variations of the bias with mass and redshift. Such studies on mass and redshift trends of B have already been carried out in weak lensing works (von der Linden et al. (2014), Hoekstra et al. (2015), Smith et al. (2016), Sereno & Ettori (2017)) or using tSZ number counts (Salvati et al. 2019) giving sometimes contradictory results. In this work we measure and use gas mass fractions from a large sample to get new independent constraints on B and its mass and redshift evolution. We also aim at investigating the role that an evolution of the bias would have on the cosmological constraints we obtain from f_{gas} data.

After describing the theoretical modelling and our cluster sample in Section 2, we detail our methods for the data analysis in Section 3. We show our results in Section 4, first focusing on the effect of assuming a varying bias on our derived cosmological constraints, then looking at the sample dependence of our results. We finally discuss our results in Section 5 and draw our conclusions in Section 6. Throughout the paper we assume a reference cosmology with $H_0 = 70 \text{ km.s}^{-1} \cdot \text{Mpc}^{-1}$, $\Omega_m = 0.3$, $\Omega_\Lambda = 0.7$.

2. Theoretical modelling and data

2.1. Gas fraction sample

The gas mass fraction is defined as the ratio of the gas mass over the total mass of the cluster,

$$f_{gas} = \frac{M_{gas}}{M_{tot}}. \quad (1)$$

Using X-ray observations, the gas mass is obtained by integrating the density profile $\rho(r)$ inside a certain radius r as shown in equation 2 below

$$M_{gas}(< r) = \int_0^r 4\pi r'^2 \rho(r') dr'. \quad (2)$$

Here, the density profile $\rho(r)$ is obtained from the electron density profile $n_e(r)$, measured from X-ray observations. We have

$$\rho(r) = \mu m_p (n_e(r) + n_p(r)), \quad (3)$$

where μ is the mean molecular weight, m_p the proton mass, n_e the electron number density and n_p the proton number density with $m_e = 1.17 m_p$ in a fully ionised gas. Using the density profile and a temperature profile $T(r)$, the total hydrostatic mass M_{HE} can be computed by solving the hydrostatic equilibrium equation shown below,

$$M_{HE}(< r) = -\frac{rk_B T(r)}{G \mu m_p} \left(\frac{d \ln \rho(r)}{d \ln r} + \frac{d \ln T(r)}{d \ln r} \right), \quad (4)$$

where k_B is the Boltzmann constant and G the gravitational constant.

Similarly to the gas mass and the hydrostatic mass, the cluster gas mass fraction is evaluated within a characteristic radius, determined by the radius of the mass measurements. We define this radius R_Δ , as the radius that encloses Δ times the critical density of the Universe, $\rho_c = 3H^2/8\pi G$. The gas content inside galaxy clusters is affected by baryonic physics, and the impact of the different astrophysical processes might depend on the considered cluster radius R_Δ . In this work, we focus on gas fractions which were taken at R_{500} , and from now on all the quantities we consider are taken at R_{500} . Note that this radius is larger than most studies using the gas fraction of galaxy clusters as a cosmological probe, which are generally carried out at R_{2500} (Allen et al. (2002), Allen et al. (2008), Allen et al. (2011), Mantz et al. (2014), Holanda et al. (2020), Mantz et al. (2022)). We briefly discuss this choice of radius in Section 5.2.2.

We computed the gas fraction for the clusters in the *Planck*-ESZ survey (Planck Collaboration et al. 2011). In particular, we consider 120 out of 189 clusters of the *Planck*-ESZ sample, for which we have follow-up X-ray observations by *XMM-Newton* up to R_{500} , which we still call the ESZ sample for simplicity. Our sample therefore spans a total mass range from $2.22 \times 10^{14} \text{ M}_\odot$ to $1.75 \times 10^{15} \text{ M}_\odot$ and redshift range from 0.059 to 0.546. We start from the gas and total masses of the clusters which were derived in Lovisari et al. (2020). We refer the reader to their work for the detailed analysis of the mass evaluation. We just stress here that the total cluster masses were obtained assuming hydrostatic equilibrium, as shown in equation 4, therefore inducing the presence of the hydrostatic mass bias. From these gas masses and hydrostatic masses we computed the gas fraction following equation 1, to find that they are within the range [0.06, 0.20]. When evaluating the uncertainty on f_{gas} , we adopt a conservative approach, using the maximum error between the

lower and upper errors of the mass measurements. We give the redshifts, gas masses, hydrostatic masses and gas fractions of the clusters from our sample in Table A.1 in appendix.

We show in Figure 1 the observed gas fraction in this sample, with respect to redshift and mass. We also compare these f_{gas} values to the universal baryon fraction $\Omega_b/\Omega_m = 0.156 \pm 0.03$ from *Planck* 2018 results (Planck Collaboration et al. 2020).

2.2. Modelling of the observed gas fraction

The hydrostatic mass is used to evaluate the total cluster mass, yet is biased low with respect to the true total mass by a factor $B = M_{\text{HE}}/M_{\text{true}}$. The measured gas mass fraction is thus :

$$f_{\text{gas,mes}} = \frac{M_{\text{gas}}}{M_{\text{HE}}} = \frac{M_{\text{gas}}}{B \times M_{\text{true}}} = \frac{1}{B} \times f_{\text{gas,true}}. \quad (5)$$

Besides the hydrostatic mass bias, the measured gas fraction depends on a variety of instrumental, astrophysical and cosmological effects. A way of quantifying these effects is to compare the gas fraction we obtain from gas mass and hydrostatic mass measurements to the theoretical (hydrostatic) gas fraction we expect from equation 6 below, from Allen et al. (2008). In this equation and in the rest of the paper, a quantity noted X^{ref} is the quantity X in our reference cosmology :

$$f_{\text{gas,Th}}(M, z) = K \frac{\Upsilon(M, z)}{B(M, z)} A(z) \left(\frac{\Omega_b}{\Omega_m} \right) \left(\frac{D_A^{\text{ref}}(z)}{D_A(z)} \right)^{3/2} - f_{*}. \quad (6)$$

Here K is an instrumental calibration correction. We take $K = 1 \pm 0.1$ from Allen et al. (2008) and discuss the soundness of this assumption in Section 5.1.1. Regarding the astrophysical contributions, $\Upsilon(M, z)$ is the baryon depletion factor, describing how baryons in clusters are depleted with respect to the universal baryon fraction and $B(M, z)$ is the hydrostatic mass bias we have discussed above. Finally Ω_b/Ω_m is the universal baryon fraction, D_A is the angular diameter distance, f_{*} is the stellar fraction, and $A(z)$ is an angular correction which we show in equation 7

$$A(z) = \left(\frac{\theta_{500}^{\text{ref}}}{\theta_{500}} \right)^\eta \simeq \left(\frac{H(z)D_A(z)}{[H(z)D_A(z)]^{\text{ref}}} \right)^\eta. \quad (7)$$

The parameter η accounts for the slope of the f_{gas} profiles enclosed in a spherical shell. Here we take $\eta = 0.442$ from Mantz et al. (2014). $A(z)$ being however very close to one for realistic models and within our range of parameters, the value of this parameter has a negligible impact on our results.

3. Methods

Our purpose in this work is to use the gas mass fraction of galaxy clusters to constrain the value of the hydrostatic mass bias, and particularly its evolution with mass and redshift. We also want to study the role of such an evolution of the bias on the subsequent cosmological constraints derived from f_{gas} data. We recall here that all constraints derived from gas mass fraction data are obtained by comparing the measured gas fraction to the theoretical gas fraction expected from equation 6, which is proportional to the universal baryon fraction. Besides this proportionality, all the other constraints are deduced as corrections needed to match the observed f_{gas} in clusters to the constant Ω_b/Ω_m . As discussed in Section 2, one of these correction terms accounts for the baryonic effects taking place in the ICM. These baryonic effects are

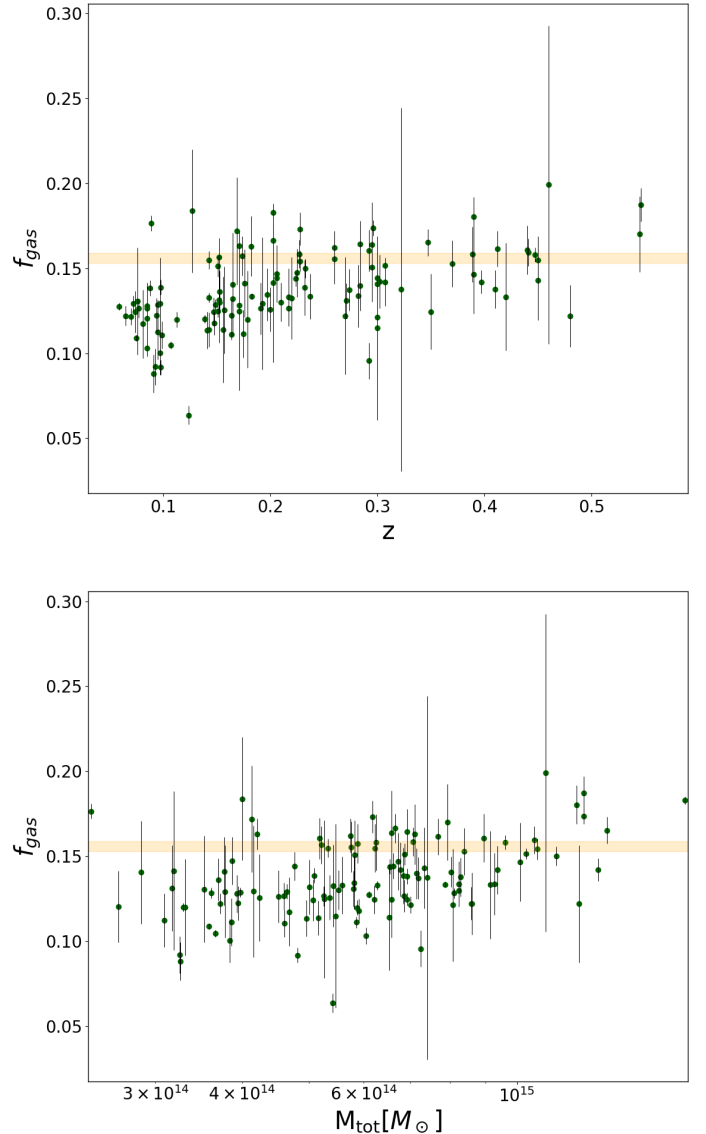


Fig. 1. Top: Gas mass fraction of *Planck*-ESZ clusters with respect to redshift. Bottom: Gas mass fraction of *Planck*-ESZ clusters with respect to cluster mass. The yellow bands in both plots mark the Planck Collaboration et al. (2020) value of $\Omega_b/\Omega_m = 0.156 \pm 0.003$.

accounted for by the depletion factor $\Upsilon(M, z)$ and the hydrostatic bias $B(M, z)$, which we are interested in. As shown in equation 6, we cannot constrain independently $B(M, z)$ and $\Upsilon(M, z)$, as the two parameters are strongly degenerated. What we have access to instead is the ratio of the two quantities, $\Upsilon(M, z)/B(M, z)$. In order to break this degeneracy and properly constrain the bias, strong constraints on the depletion factor and its evolution with mass and redshift are required. Obtaining such results is however out of the scope of this paper, and we retrieve these constraints from hydrodynamical simulations works.

The depletion factor is known to vary with mass, however this evolution is particularly strong for groups and low mass clusters ($< 2.10^{14} M_{\odot}$) while it becomes negligible at the high masses we consider (see the discussion in Section 3.1.1 of Eckert et al. (2019) based on results from The Three Hundred Project simulations (Cui et al. 2018)). Works from Planelles et al. (2013) and Battaglia et al. (2013) equally show that the depletion factor

Parameter	Bias evolution study		Sample dependence of the results	Reference
	Prior	Prior	Prior	
B_0	–	–	$\mathcal{U}(0.3, 1.7)$	–
$B(z_{CCCP}, M_{CCCP})$	$\mathcal{N}(0.780, 0.092)$	–	$\mathcal{N}(0.015, 0.005)$	1
f_*	$\mathcal{N}(0.015, 0.005)$	–	$\mathcal{N}(0.015, 0.005)$	2
Υ_0	$\mathcal{N}(0.79, 0.03)$	–	$\mathcal{N}(0.79, 0.03)$	3
K	$\mathcal{N}(1, 0.1)$	–	$\mathcal{N}(1, 0.1)$	4
σ_f	$\mathcal{U}(0, 1)$	–	$\mathcal{U}(0, 1)$	–
h	$\mathcal{N}(0.674, 0.005)$	–	$\mathcal{N}(0.674, 0.005)$	5
Ω_b/Ω_m	$\mathcal{U}(0.05, 0.3)$	–	$\mathcal{N}(0.156, 0.003)$	5
Ω_m	$\mathcal{U}(0.01, 1)$ (CB, VB) or $\mathcal{N}(0.315, 0.007)$ (VB + Ω_m)	–	$\mathcal{N}(0.315, 0.007)$	5
α	Fixed at 0 (CB) or $\mathcal{U}(-2, 2)$ (VB, VB + Ω_m)	–	$\mathcal{U}(-2, 2)$	–
β	Fixed at 0 (CB) or $\mathcal{U}(-2, 2)$ (VB, VB + Ω_m)	–	$\mathcal{U}(-2, 2)$	–

References. (1) Hoekstra et al. (2015); (2) Eckert et al. (2019); (3) Planelles et al. (2013); (4) Allen et al. (2008); (5) Planck Collaboration et al. (2020).

Table 1. Set of priors used in our analysis. A prior noted $\mathcal{U}(l, u)$ is a uniform prior of lower bound l and upper bound u , while a prior noted $\mathcal{N}(\mu, \sigma)$ is a gaussian prior of mean μ and standard deviation σ .

is constant with redshift when working at R_{500} . Throughout the paper we thus assume a constant depletion factor with mass and redshift $\Upsilon_0 = 0.79 \pm 0.03$, based on hydrodynamical simulations from Planelles et al. (2013).

3.1. Bias evolution modelling

In order to analyse a possible mass and redshift evolution of the mass bias, we consider a power-law evolution for the hydrostatic bias, with pivot masses and redshift set at the mean values of the considered cluster sample :

$$B(z, M) = B_0 \left(\frac{M}{\langle M \rangle} \right)^\alpha \left(\frac{1+z}{\langle 1+z \rangle} \right)^\beta \quad (8)$$

$$-2 \ln \mathcal{L} = \sum_i \left\{ \ln 2\pi s_i^2 + \frac{\left[f_{gas,i} - K \frac{\Upsilon_0}{B_0} \left(\frac{M_i}{\langle M \rangle} \right)^{-\alpha} \left(\frac{1+z_i}{\langle 1+z \rangle} \right)^{-\beta} A(z_i, h, \Omega_m) \frac{\Omega_b}{\Omega_m} \left(\frac{D_A^{ref}(z_i)}{D_A(z_i, h, \Omega_m)} \right)^{3/2} + f_* \right]^2}{s_i^2} \right\}, \quad (9)$$

where

$$s_i^2 = \sigma_i^2 + f_{gas,Th}^2 \sigma_f^2, \quad (10)$$

with σ_i the uncertainties on the gas fraction data, and $f_{gas,Th}$ the gas fraction expected from equation 6. The parameter σ_f is the intrinsic scatter of the data, which we treat as a free parameter.

3.2. Free cosmology study

In the first part of our analysis we simply assess the necessity to consider an evolving bias, by looking at the impact of assuming such a variation on the subsequent cosmological constraints. To do so, we compare the posterior distributions in three different cases :

- In the first case we let free the baryon fraction Ω_b/Ω_m , the matter density Ω_m , and the parameters accounting for the variation of the bias α , β and B_0 . We will refer to this scenario as "VB".

with B_0 an amplitude.

We chose this model for the sake of simplicity following what is done in Salvati et al. (2019), as the exact dependence of B on mass and redshift is not known. In Section 5.1.2 we discuss the role of this parametrization by comparing our results with a linear evolution of B , and find results similar to those of the power-law description.

The complete likelihood function thus writes :

- In the second case we let free only the cosmological parameters and fix the bias parameters $\alpha = 0$ and $\beta = 0$, resulting in a constant bias at the value B_0 . This scenario will be noted in the rest of the paper as "CB".
- Due to a degeneracy between β and Ω_m which we discuss later on, we also look at our results when leaving the set of parameters $(B_0, \alpha, \beta, \Omega_b/\Omega_m)$ free but assuming a prior on Ω_m , in order to break this degeneracy and constrain β more accurately. We call this scenario "VB + Ω_m ".

The set of parameters for which we assume flat priors in this part of the study is thus $(B_0, \alpha, \beta, \Omega_b/\Omega_m, \Omega_m, \sigma_f)$, as we show in the first column of Table 1. This work is performed on the entirety of our cluster sample, for which our mean mass and redshift are :

$$(M_{full}, z_{full}) = (6.42 \times 10^{14} M_\odot, 0.218) \quad (11)$$

Throughout this whole part of the analysis, we consider a prior on the total value of the bias for a certain cluster mass and redshift, taken from the CCCP analysis Hoekstra et al. (2015) :

$$B(z_{CCCP}, M_{CCCP}) = 0.780 \pm 0.092,$$

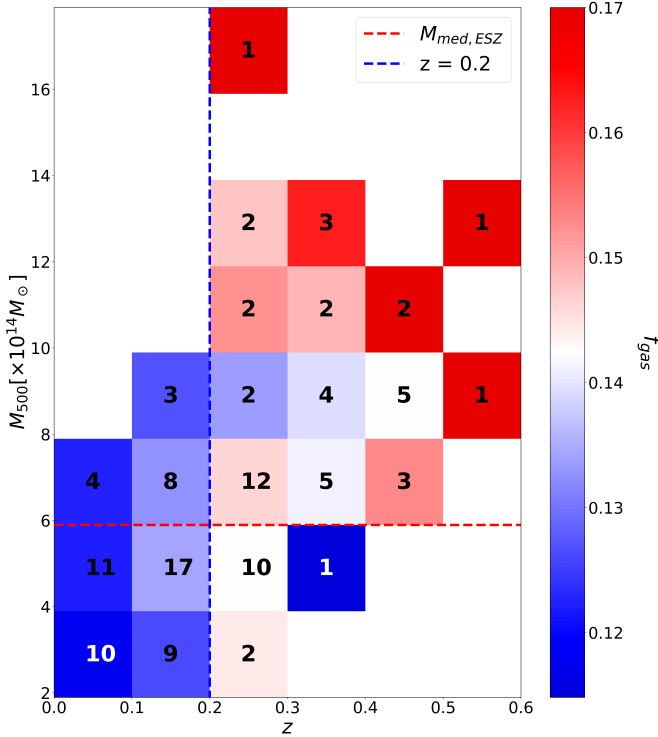


Fig. 2. Binned mass-redshift plane of the *Planck*-ESZ sample. Inside each bin we compute the mean value of f_{gas} . We show the number of clusters included in each bin and mark the delimitation of each subsample.

where $z_{\text{CCCP}} = 0.246$ and $M_{\text{CCCP}} = 14.83 \times 10^{14} h^{-1} M_{\odot}$ are the mean mass and redshift for the CCCP sample.

3.3. Sample dependence tests

In a second part, we look into possible sample dependencies of our results regarding the value of the bias parameters B_0 , α and β . To that end we focus on different subsamples inside the main sample, based on mass and redshift selections. Matching the selection from weak lensing studies like the CoMALIT (Sereno & Ettori 2017) or LoCuSS (Smith et al. 2016) studies, we operate a redshift cut at $z = 0.2$, differentiating clusters that are above or below this threshold value. This choice was also motivated by the results from Salvati et al. (2019), investigating the hydrostatic mass bias from the perspective of tSZ number counts. Their study showed that the trends in the mass bias depended on the considered redshift range, with results changing when considering only clusters with $z > 0.2$. We also perform a mass selection, differentiating between the clusters that are above or below the median mass of the sample $M_{\text{med}} = 5.89 \times 10^{14} M_{\odot}$.

In summary, the samples we are considering in this study are the following :

- The full sample of 120 clusters, with the mean mass and redshift given previously in equation 11.
- Clusters with $z < 0.2$ and $M < 5.89 \times 10^{14} M_{\odot}$. We consider them in the "*Low Mz*" subsample, which contains 47 clusters. The mean mass and redshift are

$$(M_{\text{lowMz}}, z_{\text{lowMz}}) = (4.26 \times 10^{14} M_{\odot}, 0.126) \quad (12)$$

- Clusters with $z > 0.2$ and $M > 5.89 \times 10^{14} M_{\odot}$. We consider them in the "*High Mz*" subsample, which contains 45

clusters. The mean mass and redshift are

$$(M_{\text{highMz}}, z_{\text{highMz}}) = (8.86 \times 10^{14} M_{\odot}, 0.333) \quad (13)$$

We do not consider the "Low z - high M " and "High z - low M " subsamples as by construction they do not contain enough clusters (respectively 15 and 13) to obtain meaningful results. For illustration purposes we show in Figure 2 the binned mass-redshift plane of our sample, with the delimitation of the different subsamples. Inside each bin we compute the mean value of f_{gas} if at least one cluster is inside the bin.

To carry out this study of the sample dependence we compare the posterior distributions obtained when running our MCMC on the three aforementioned samples independently. Note that we keep the prior on Ω_m for this part of the study, and that we add a prior on Ω_b/Ω_m . This choice is motivated by the presence of a degeneracy between the baryon fraction and the amplitude of the bias B_0 . This degeneracy is broken in the first part of the analysis by assuming a prior on the total value of the bias. However, when trying to compare all the bias parameters between samples (including the amplitude), we do not wish to be dependant on such a prior. The universal baryon fraction being well known and constrained, such a prior is a convenient way to break the degeneracy between Ω_b/Ω_m and B_0 and still obtain meaningful results on the value of all the bias parameters. The set of parameters following flat priors in this part of the study is thus $(B_0, \alpha, \beta, \sigma_f)$, as we show in the second column of Table 1.

In brief, we adopt the list of priors given in Table 1 to constrain the parameters used to describe our f_{gas} data. We fit our model in equation 6 to the f_{gas} data with an MCMC approach using the sampler emcee (Foreman-Mackey et al. 2013). Note that the prior we consider on $f_* = 0.015 \pm 0.005$ coming from Eckert et al. (2019) has close to no effect on our final results, as this term in equation 6 is almost negligible.

4. Results

4.1. Bias evolution study

In the first section of this analysis we intend on studying the possibility of an evolution of the hydrostatic mass bias with cluster mass and redshift. To that purpose we compare the cosmological constraints obtained on the full sample when considering a constant bias to those obtained when leaving the bias free to vary. Our results are summed up in Figure 3 and in Table 2.

In the VB case, i.e. when leaving the set of parameters $(B_0, \alpha, \beta, \Omega_b/\Omega_m, \Omega_m, \sigma_f)$ free with a prior on the total value of B , we show that a mass independent bias seems to be favoured, with $\alpha = -0.047 \pm 0.037$ compatible with 0, albeit peaking slightly lower. We also show that our derived Ω_b/Ω_m is fully compatible with the *Planck* Collaboration et al. (2020) value, as we obtain $0.163^{+0.025}_{-0.036}$. We cannot however bring such constraints on β and Ω_m , as these two parameters are heavily degenerated. We zoom in on this degeneracy in Figure 4 and show that higher values of β call for higher values of Ω_m . This degeneracy can be explained by the fact that both parameters are encoding a redshift dependence of the gas fraction. Indeed, Ω_m intervenes in the computation of $D_A(z)$ and $H(z)$, which entirely drive the sensitivity of f_{gas} to cosmology. We thus argue that this degeneracy between β and Ω_m that we show here in a simple Flat- Λ CDM model could also be observed between β and any other cosmological parameter, as long as they appear in the computation of $D_A(z)$ or $H(z)$. On a side note, we show a slight degeneracy between the baryon fraction Ω_b/Ω_m and β , with a lower Ω_b/Ω_m implying a higher, closer to 0 β . This degeneracy is caused by

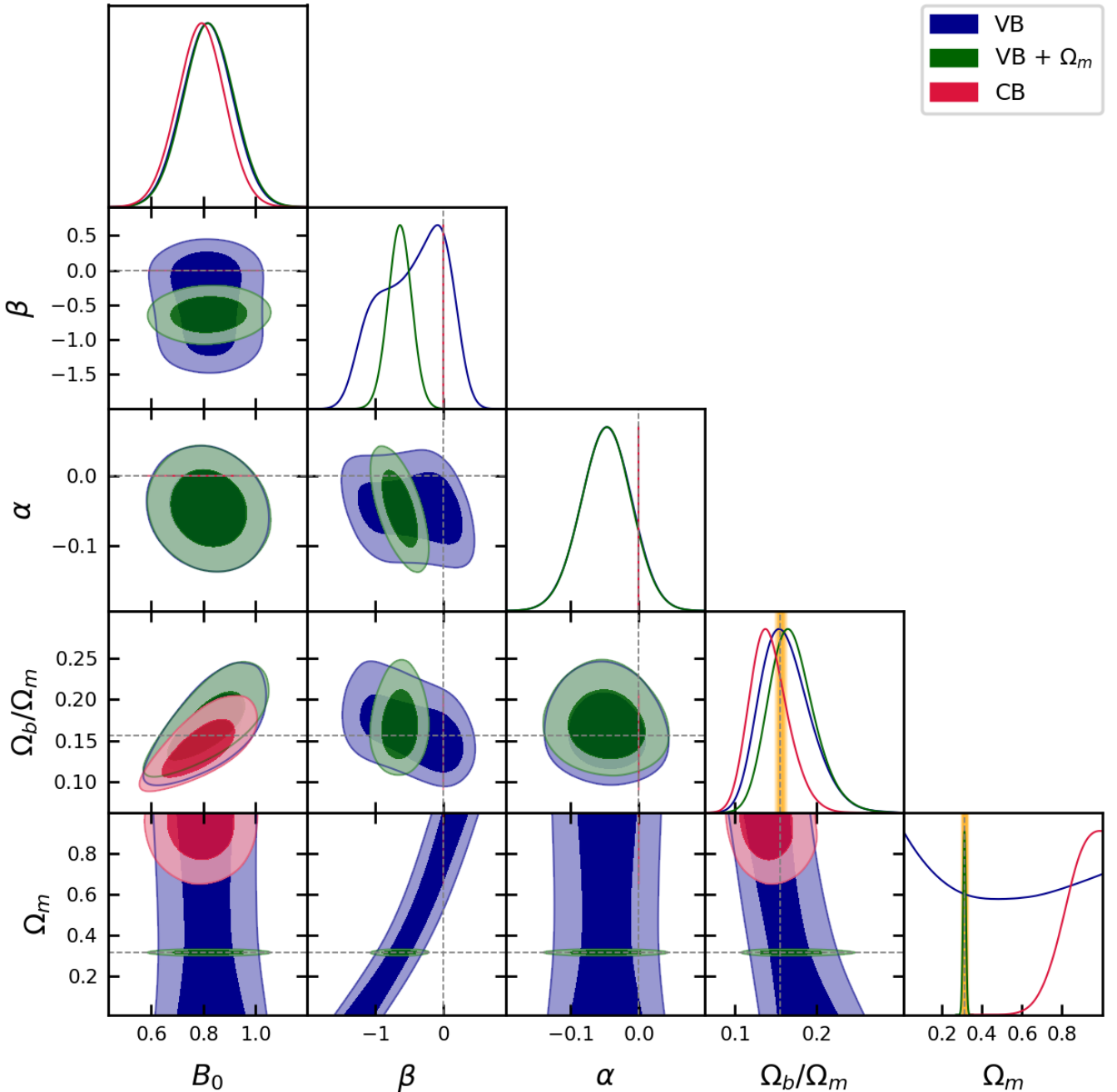


Fig. 3. 1D and 2D posterior distributions for the CB, VB, and VB + Ω_m scenarios. The contours mark the 68% and 95% confidence level (c.l.). The grey dashed lines highlight reference values for $(\alpha, \beta, \Omega_b/\Omega_m, \Omega_m) = (0, 0, 0.156, 0.315)$. The orange bands mark the Planck Collaboration et al. (2020) values for Ω_b/Ω_m and Ω_m at 2σ c.l.

the combined effect of the degeneracy between β and Ω_m , and the degeneracy between Ω_b/Ω_m and Ω_m , which is expected and which we also show in Figure 3.

As the matter density Ω_m has been strongly constrained in a number of works, we chose to assume the Planck Collaboration et al. (2020) prior shown in Table 1 on this parameter to break its degeneracy with β , in the VB + Ω_m scenario. The effect of this prior is negligible on the constraints on α and Ω_b/Ω_m , as we obtain $\alpha = -0.047 \pm 0.037$ and $0.171^{+0.023}_{-0.031}$, fully compatible with the results obtained without this prior. On the other hand the use of this prior allows us to constrain β . We show that the hy-

drostatic bias seems to show a strong redshift dependence, with $\beta = -0.64 \pm 0.17$. This value of $\beta < 0$ would mean a value of B decreasing with redshift, that is to say more and more biased masses towards higher redshifts. We also note a slight degeneracy between α and β , but this is most probably due to selection effects of the sample. As the higher redshift clusters tend to mostly have higher masses (see Figure 2), a redshift trend of the bias could then be interpreted as a slight mass trend, explaining this degeneracy.

The effect of assuming a constant bias ($\alpha = \beta = 0$) in the CB case does not have a strong impact on our constraints on Ω_b/Ω_m ,

Parameter	CB	VB	VB + Ω_m
B_0	0.791 ± 0.091	0.817 ± 0.095	0.821 ± 0.096
α	0	-0.047 ± 0.037	-0.047 ± 0.037
β	0	$-0.45^{+0.60}_{-0.38}$	-0.64 ± 0.17
Ω_b/Ω_m	$0.142^{+0.020}_{-0.026}$	$0.163^{+0.025}_{-0.036}$	$0.171^{+0.023}_{-0.031}$
Ω_m	> 0.849	—	0.315 ± 0.007

Table 2. Constraints obtained on bias and cosmological parameters in the CB, VB and VB + Ω_m scenarios. The uncertainties are given at 68% c.l.

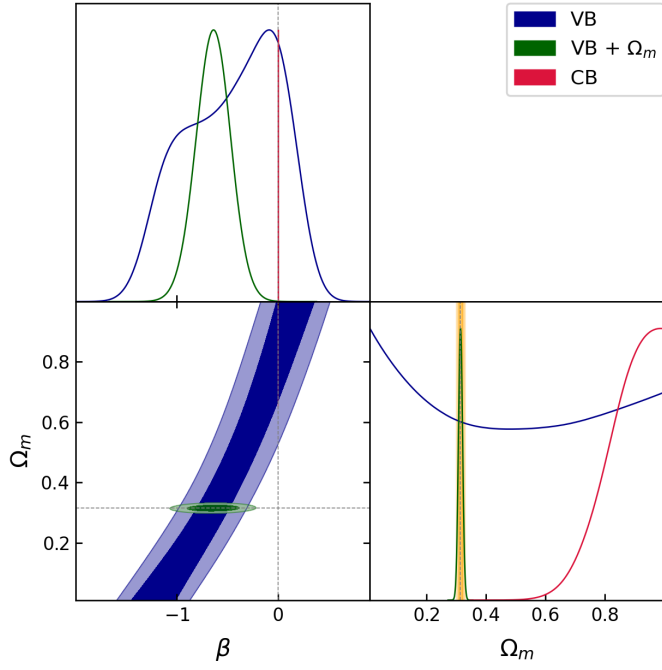


Fig. 4. Posterior distributions showing the degeneracy between β and Ω_m . The contours mark the 68% and 95% c.l. The grey dashed lines highlight reference values for $(\beta, \Omega_m) = (0, 0.315)$. The orange band marks the [Planck Collaboration et al. \(2020\)](#) value for Ω_m at 2σ c.l.

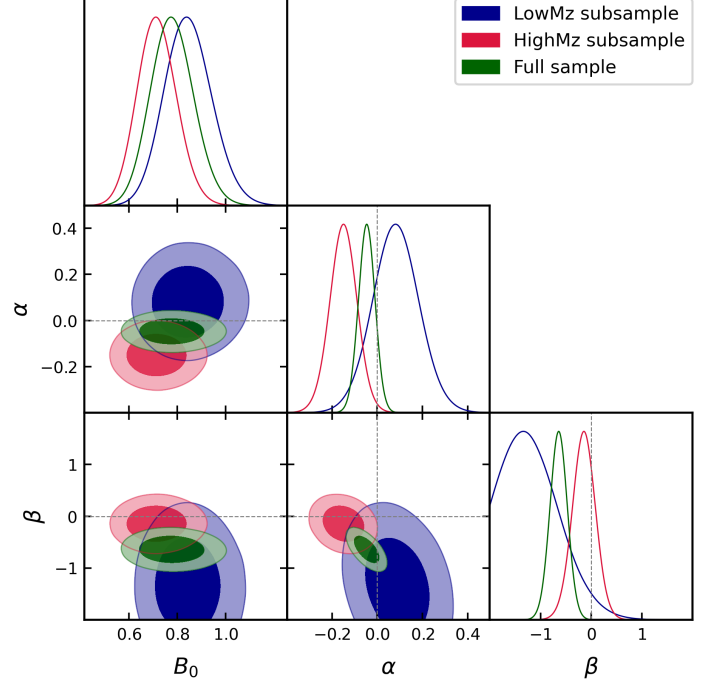


Fig. 5. 1D and 2D posterior distributions for the bias parameters in the three mass and redshift selected samples. The levels of the contours mark the 68% and 95% confidence levels. The grey dashed lines mark the reference values $(\alpha, \beta) = (0, 0)$

which peaks just slightly below the *Planck* value but remains compatible, with $\Omega_b/\Omega_m = 0.142^{+0.020}_{-0.026}$. B_0 is slightly below yet compatible with the value found in the varying bias case, with $B_0 = 0.791 \pm 0.091$. This is simply caused by the fact that for a constant bias the amplitude B_0 is now completely determined by the total value of the bias $B(z_{CCCP}, M_{CCCP})$. On the other hand, due to the degeneracy between β and Ω_m , imposing no redshift evolution of the bias requires a very high matter density, resulting in $\Omega_m > 0.894$, fully incompatible with the *Planck* value. Such a high matter density is not expected in current standard cosmology and is totally aberrant.

As such, we show that we need to assume an evolution of the hydrostatic mass bias, at least in redshift, to properly describe our f_{gas} data. In the rest of our study we focus on exploring the bias evolution. We thus consider only the VB + Ω_m scenario, to be able to constrain β despite its degeneracy with the matter density. We also assume a [Planck Collaboration et al. \(2020\)](#) prior on Ω_b/Ω_m , as the universal baryon fraction is degenerated with the total value of the bias (see equation 6). The bias parameters (B_0, α, β) are thus left free, and we chose not to use a prior on the total value of B anymore.

4.2. Sample dependence of the results

If an evolution of the bias seems necessary to properly constrain cosmological parameters using f_{gas} data at R_{500} , the strength of this evolution might differ depending on the masses and redshifts of the clusters we consider. We thus repeat the previous study, this time focusing only on the bias parameters, on the previously defined *LowMz* and *HighMz* subsamples in addition to the full sample. We recall that in this section, we are considering the VB + Ω_m scenario, with an additional prior on Ω_b/Ω_m . The summary of our results is given in Table 3 and Figures 5 and 6.

Our results when considering the full sample are, as expected, the same as when adopting flat priors on the cosmological parameters. The only slight exception is B_0 , peaking slightly lower due to the absence of a prior on the total bias. We find an amplitude $B_{0,\text{full}} = 0.779 \pm 0.089$. The parameters accounting for the bias evolution remain unchanged, with $\alpha_{\text{full}} = -0.047 \pm 0.037$ and $\beta_{\text{full}} = -0.64 \pm 0.17$. We thus remain compatible with no mass evolution of the bias but still find a strong hint for a redshift dependence.

If all subsamples provide compatible values for the amplitude with $B_{0,\text{lowMz}} = 0.846^{+0.091}_{-0.10}$, $B_{0,\text{HighMz}} = 0.716 \pm 0.081$ and $B_{0,\text{full}} = 0.779 \pm 0.089$, this cannot be said regarding α and β . Indeed, if the study of the full sample seems to sug-

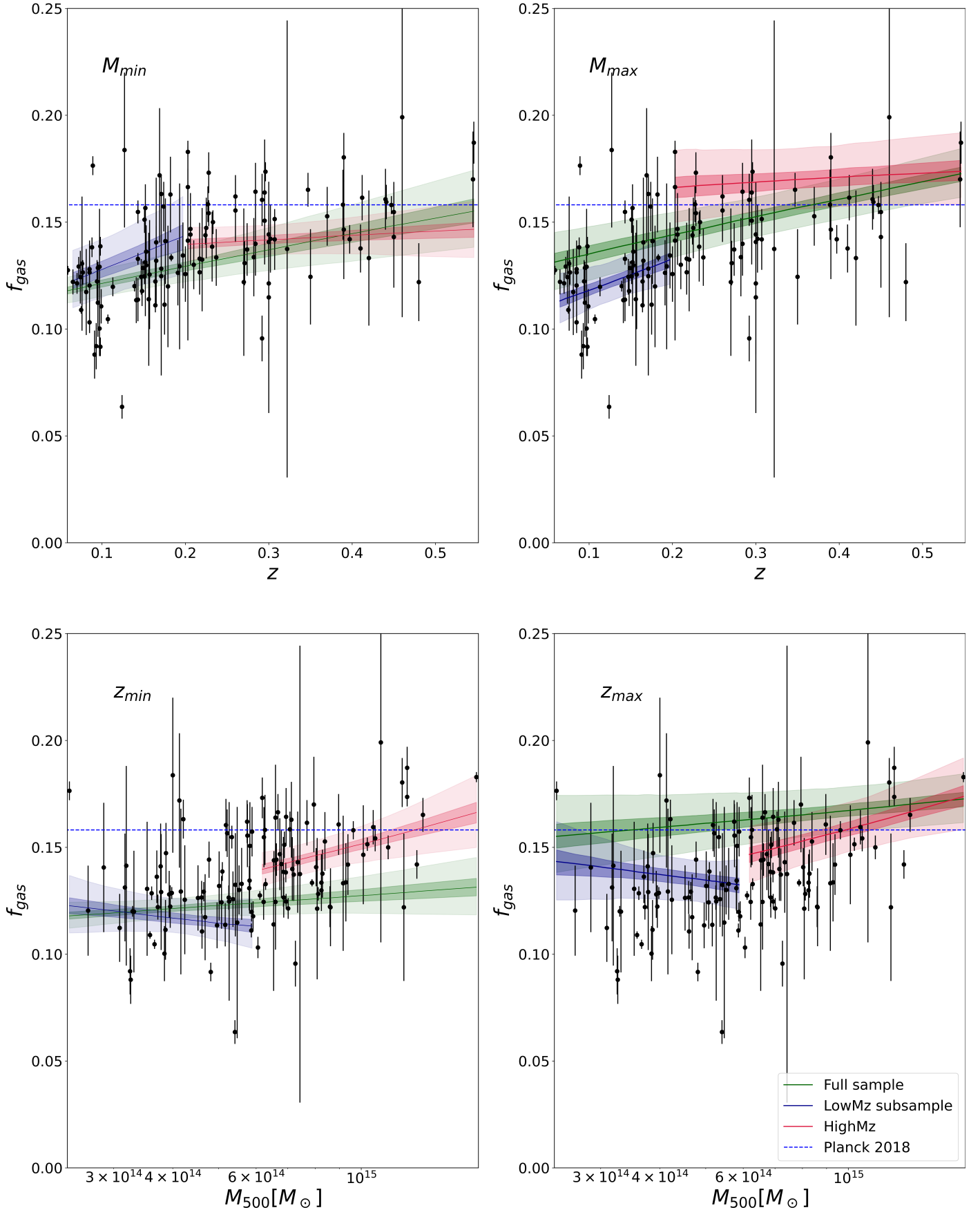


Fig. 6. Fits obtained from our analysis, for the different mass and redshift selected samples. The results in the top two panels are represented with respect to redshift at constant mass (respectively minimal and maximal masses of the full sample), while the bottom two panels are the results presented with respect to mass, at fixed redshift (respectively minimal and maximal redshifts of the full sample). The shaded areas around the curves mark the 68% and 95% confidence levels. The blue dashed line marks the reference value $\Omega_b/\Omega_m = 0.156$

Parameter	LowMz subsample	HighMz subsample	Full sample
B_0	$0.846^{+0.091}_{-0.10}$	0.716 ± 0.081	0.779 ± 0.089
α	0.08 ± 0.10	-0.150 ± 0.061	-0.047 ± 0.037
β	$-1.14^{+0.33}_{-0.73}$	-0.14 ± 0.23	-0.64 ± 0.17

Table 3. Constraints obtained on the bias parameters depending on the considered sample. The uncertainties are given at 68% c.l.

gest no mass evolution and a mild redshift trend of the bias, we observe the reverse behaviour in the *HighMz* subsample. With $\alpha_{highMz} = -0.150 \pm 0.061$ and $\beta_{HighMz} = -0.14 \pm 0.23$, the preferred scenario would be the one of B constant with redshift, yet decreasing with cluster mass. On the other end of the mass-redshift plane, the results show exactly the opposite evolution, in agreement with the constraints from the full sample but aggravating the trends. With $\alpha_{LowMz} = 0.08 \pm 0.10$ and $\beta_{LowMz} = -1.14^{+0.33}_{-0.73}$, we show we are fully compatible with no mass evolution of the bias, even with the posterior of α peaking slightly above 0 contrary to the other samples. More importantly, we show a strong decreasing trend of B with redshift, as we obtain β peaking below -1. We note that the posterior distribution for this subsample is quite wider than for the full sample or the *HighMz*. This is due to the smaller mass and redshift range of this sample (see Figure 2), diminishing its constraining power with respect to the other two selections. This is however sufficient to highlight a redshift dependence of the bias when considering the least massive clusters of our sample at the lowest redshifts.

In Figure 6 we show what these values of the bias parameters translate to in terms of gas fraction with respect to redshift and mass. We show these fits computed at $[M_{min}, M_{max}]$ with z free, and at $[z_{min}, z_{max}]$ with M free, taking into account the uncertainties at 68% and 95% c.l. We first notice what was highlighted in the contours of Figure 5, which is that the results obtained for the full sample mainly fall in between the two extreme cases of the *LowMz* and *HighMz* subsamples. Secondly we show that the incompatibility between the two smaller subsamples is well visible in the result of the fits. In the bottom two panels showing the $f_{gas}(M)$ relation, the *LowMz* and *HighMz* even seem to exhibit opposite trends, similarly to what was seen in Figure 5. Finally we note an offset in the relative positions of the curves for the two subsamples, depending on mass and redshift. This is simply due to the fact that our model describes a simultaneous evolution of the bias both with mass and redshift, which happens to be non-zero in our case.

In summary we thus claim to find strong evidence for a sample dependence of our results regarding the mass and redshift evolution of the hydrostatic mass bias. Such sample dependence had already been noted in other works studying the evolution of the bias using tSZ cluster counts, but not when using f_{gas} data.

5. Discussion

As we have shown in the previous section, considering an evolution of the bias seems to be necessary to infer sensible cosmological constraints. On the other hand, the variation of the bias that we measure is very dependent on the sample we consider, as we show different trends of the bias depending on mass and redshift selections inside our main sample. We discuss these results here, trying to take into account all the systematic effects that could appear and bias our results. We also compare our findings to previous studies which focused on the bias and its evolution, from different probes.

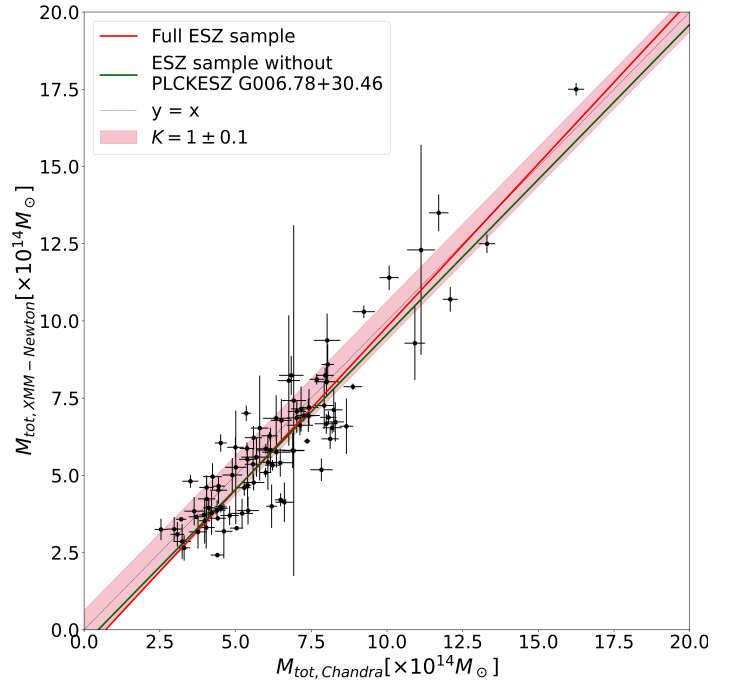


Fig. 7. Comparison of the total masses inside the *Planck*-ESZ sample between XMM-Newton and Chandra.

5.1. Possible sources of systematic effects

5.1.1. Instrumental calibration effects

All of the masses used in this work were taken from Lovisari et al. (2020), where the authors used XMM-Newton observations. Possible calibration effects may have impacted the mass measurements in their work and induced biases (see e.g. Mahdavi et al. (2013) or Schellenberger et al. (2015)). This effect has been taken into account under the form of a $K = 1.0 \pm 0.1$ parameter in our analysis, but we try here to check if this assumption is sound. The clusters of the *Planck*-ESZ sample have also been observed using Chandra, in Andrade-Santos et al. (2021). From their work we retrieve their total masses and compare them to the XMM-Newton masses. The result of the comparison is shown in Figure 7. We perform a fit of the point cloud using a simple orthogonal distance regression method with a linear model. Similarly to the model we defined in equation 8 when studying the evolution of the bias, we set a pivot to the mean value of the Chandra masses, $\langle M_{Chandra} \rangle = 6.32 \times 10^{14} M_{\odot}$. Note that the results we present below do not change when putting the pivot at the median mass instead of the mean. By doing this we obtain the following relation :

$$M_{tot,XMM} = (1.06 \pm 0.04) M_{tot,Chandra} - (0.75 \pm 0.10) \times 10^{14} M_{\odot} \quad (14)$$

This relation might imply not only that the masses from Chandra could be biased low with respect to XMM-Newton, with a non-zero offset, but more importantly that the calibration bias could exhibit a mass-dependent behaviour. This could have an effect

regarding the mass trends of the hydrostatic mass bias. We however note that this mass dependence seems to be driven by the most massive cluster of the sample, PLCKESZ G006.78+30.46, or A2163. Indeed, with small error bars and being the only cluster in this region of the high-mass end of the sample, this cluster might artificially draw the mass dependence of the calibration bias to non-zero values. In addition, this cluster is currently undergoing merger activity and is the hottest cluster of the Abell catalogue (Maurogordato et al. 2008). As the difference between *Chandra* and *XMM-Newton* temperatures increase with cluster temperature (Schellenberger et al. 2015), and the cluster masses are measured using temperature profiles, this cluster in particular is not well suited to measure a global difference in the masses from the two instruments. We therefore perform the exact same fitting method but after removing PLCKESZ G006.78+30.46 from our sample, and show the results as the green line in Figure 7. We obtain the following relation :

$$M_{\text{tot},XMM} = (1.00 \pm 0.05)M_{\text{tot},Chandra} - (0.47 \pm 0.10) \times 10^{14} M_{\odot} \quad (15)$$

We show this time that we are fully compatible with a mass-independent mass calibration bias. We still however observe an offset, with the masses from *XMM-Newton* being globally lower than the *Chandra* masses. This result had already been shown previously (see Appendix D of Schellenberger et al. (2015)). This offset is however well accounted for by the 10% uncertainty we allow in the K prior in the majority of the sample. 34 clusters, (roughly 28% of the main sample) are laying outside the 10% tolerance allowed by the prior. They however remain within the 20% tolerance. We however point out to the reader that this comparison has been carried out only on the total masses, while our study focused on gas mass fraction. To be able to fully rule out possible biases from instrumental effects we would need to compare the gas mass fractions obtained from both observations rather than the total masses. Unfortunately as we do not have access to the gas masses from the *Chandra* observations, we can only assume that the compatibility we see for M_{tot} stays true for f_{gas} . We therefore assume that if calibration biases are affecting our study, they have only minor effects on our results.

5.1.2. Role of the parametrization

In a previous work from Wicker et al. (2022) we investigated the evolution of B with redshift, using a linear parametrization for the evolution of the bias

$$B(z) = B_0 + B_1(z - \langle z \rangle) \quad (16)$$

instead of a power-law. We compare here the results given by this choice of parametrization to the results we got for a power-law model. In this comparison of the linear case with the power law case we focus on the redshift dependence, as we did not find strong evidence for a mass evolution of the bias in the majority of our samples. We show in Figures 8, 9 and in Table 4 that the results are qualitatively consistent between the power-law and linear descriptions. Indeed in both cases when considering the $VB + \Omega_m$ scenario we observe a strong sample dependence of the results. As a matter of fact, we show in Figure 8 that the low redshift and low mass clusters strongly favour a non-zero slope $B_1 = -0.79^{+0.31}_{-0.53}$. On the high end of the mass-redshift plane we however find consistent results with the power-law case, with results compatible with no redshift evolution of B , as we find $B_1 = -0.12^{+0.11}_{-0.15}$. Our estimates of B_0 are also consistent between the power-law case and the linear case for

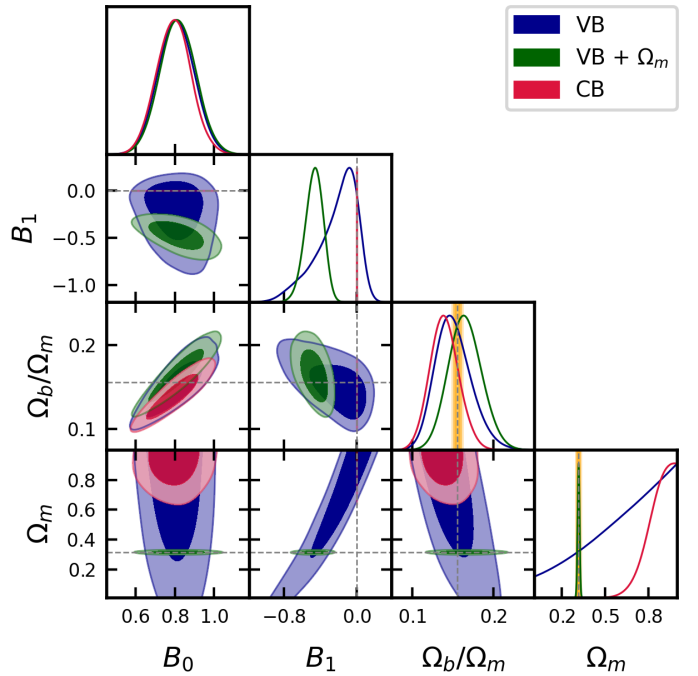


Fig. 8. 1D and 2D posteriors obtained when comparing the CB, VB and $VB + \Omega_m$ scenarios with a linear parametrization. The contours mark the 68% and 95% c.l. and the grey dashed lines highlight reference values for $(B_1, \Omega_b/\Omega_m, \Omega_m) = (0, 0.156, 0.315)$. The orange bands mark the Planck Collaboration et al. (2020) values for Ω_b/Ω_m and Ω_m at 2σ c.l.

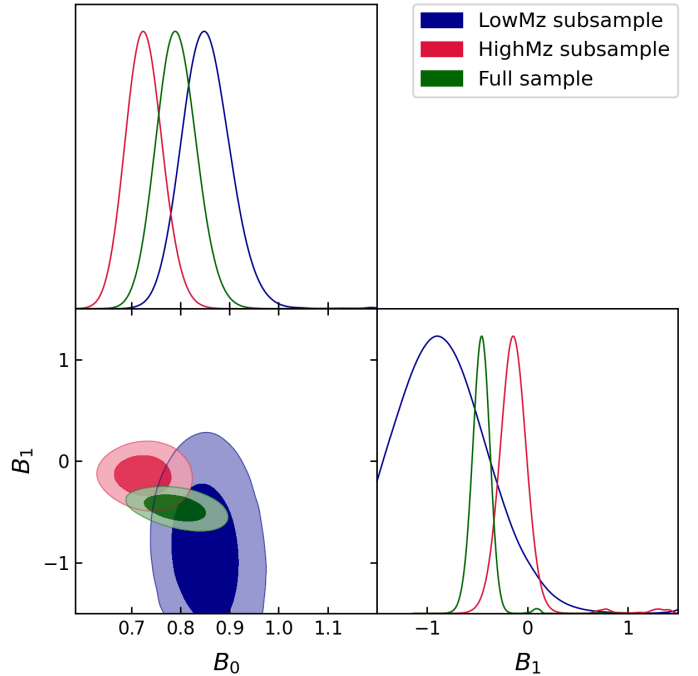


Fig. 9. 1D and 2D posteriors obtained when comparing the bias parameters derived for the three samples, when considering a linear evolution of the bias. The contours mark the 68% and 95% c.l.

each subsample respectively, as we find $B_{0,\text{lowMz}} = 0.857^{+0.041}_{-0.056}$, $B_{0,\text{highMz}} = 0.745^{+0.018}_{-0.059}$ and $B_{0,\text{full}} = 0.799^{+0.033}_{-0.050}$.

When studying the VB scenario, we still observe the strong degeneracy between the term accounting for the redshift evolution of B (here, B_1) and Ω_m . This explains why we once again

	B_0	B_1	Ω_b/Ω_m	Ω_m
CB	0.795 ± 0.088	0	0.140 ± 0.018	> 0.843
VB	0.807 ± 0.092	$-0.22^{+0.28}_{-0.13}$	$0.151^{+0.019}_{-0.025}$	–
VB + Ω_m	0.816 ± 0.092	$-0.47^{+0.11}_{-0.09}$	$0.165^{+0.019}_{-0.022}$	0.315 ± 0.007 (<i>prior</i>)
LowMz subsample	$0.857^{+0.041}_{-0.056}$	$-0.79^{+0.31}_{-0.53}$	0.156 ± 0.003 (<i>prior</i>)	0.315 ± 0.007 (<i>prior</i>)
HighMz subsample	$0.745^{+0.058}_{-0.059}$	$-0.12^{+0.11}_{-0.15}$	0.156 ± 0.003 (<i>prior</i>)	0.315 ± 0.007 (<i>prior</i>)
Full sample	$0.799^{+0.033}_{-0.050}$	$-0.456^{+0.08}_{-0.09}$	0.156 ± 0.003 (<i>prior</i>)	0.315 ± 0.007 (<i>prior</i>)

Table 4. Constraints obtained on bias and cosmological parameters, when assuming a linear parametrization. The uncertainties are given at 68% c.l. We remind that when investigating the sample dependence (second part of the table), we are considering the VB + Ω_m scenario with a prior on Ω_b/Ω_m

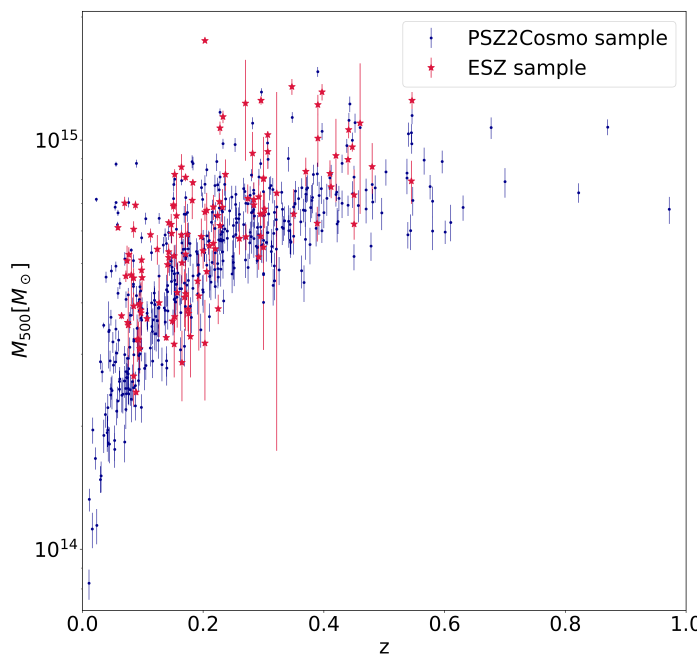


Fig. 10. Comparison between the PSZ2Cosmo sample used in [Salvati et al. \(2019\)](#) and the *Planck*-ESZ sample.

obtain aberrant values of Ω_m when considering the CB scenario. This compatibility between the qualitative results given by both parametrizations would hint at the fact that our results are not dominated by our choice of model for the bias evolution.

5.2. Comparison with other studies

5.2.1. Mass and redshift trends of the bias

We show in this work a strong sample dependence of our results, with different mass and redshift variations of the bias depending on the mass and redshift range of the subsample. We show that for low redshift and low mass clusters, the bias tends to stay constant with mass, while it increases towards higher redshift. The reverse behaviour is observed in the case of high masses and high redshift clusters, with a bias constant with redshift but slightly increasing with the mass of the objects. This sample dependence had already been noted in [Salvati et al. \(2019\)](#), where the authors used tSZ number counts on the cosmology sample of the PSZ2 catalog. The authors indeed noted a non-zero trend of the bias with redshift when considering their complete sample, that disappeared when considering only the clusters above $z = 0.2$. We however note that the compatibility of our results with theirs

regarding the mass and redshift trends depend on the considered subsample of clusters. We observe the same behaviour regarding the value of the constant term of the bias B_0 , with compatible results for the high redshift clusters but incompatible ones when considering the full sample. One might argue that these differences come from different choices of priors in the two studies. Indeed when investigating sample dependencies we do not assume any prior on the bias parameters and consider priors on cosmology, while [Salvati et al. \(2019\)](#) assume a prior on the total value of the bias, and let their cosmological parameters free. This however might not have such a strong impact, as in the first part in the analysis we let cosmological parameters free and put a prior on the total value of the bias, and we do not see significant deviations in the value of B_0 between the two cases. These differences are actually most probably due to differences between the clusters considered in the two studies, as the clusters from the ESZ sample have globally higher mass at equivalent redshift than the PSZ2Cosmo sample considered in their study, as we show in Figure 10. If anything, this could be yet another indication of the strong sample dependence of the results we show.

Our results however are consistent with other weak lensing studies among which are Weighting the Giants (WtG, [von der Linden et al. \(2014\)](#)) or CCCP ([Hoekstra et al. 2015](#)), which show a mild decreasing trend in mass for B when considering high redshift ($z_{WtG} = 0.31$, $z_{CCCP} = 0.246$) and high mass ($M_{500,WtG} = 13.58 \times 10^{14} M_\odot$, $M_{500,CCCP} = 10.38 \times 10^{14} M_\odot$) clusters. More recent works like the X-ray study X-COP ([Eckert et al. 2019](#)) also seem to show a possible mass dependent bias, with a decreasing trend of B . The weak-lensing studies LoCuSS ([Smith et al. 2016](#)) and CoMALIT ([Sereno & Ettori 2017](#)) both find decreasing trends of B with redshift, in agreement with this work, for clusters in the mass and redshift range of our sample ($z_{LoCuSS} = 0.22$, $M_{LoCuSS} = 6.8 \times 10^{14} M_\odot$).

5.2.2. Discussing the choice of a sample at R_{500}

In this work we focus on gas fractions taken at R_{500} , which is larger than most works using f_{gas} as a cosmological probe, carried out at R_{2500} . The choice of R_{2500} is generally motivated by the low scatter of the gas fraction data around those radii (see [Mantz et al. \(2014\)](#) and references therein), allowing for more precise cosmological constraints. The scatter f_{gas} in data is larger at R_{500} , however this inconvenient is balanced by the stability of the depletion factor Υ at this radius. Indeed as shown by the hydrodynamical simulations from [Planelles et al. \(2013\)](#), the value of Υ does not vary much with the radius when one measures it around R_{500} . This reduces the possibility of a biased estimation of the depletion due to incorrect determinations of R_{500} . On the other hand Υ starts to decrease in the vicinity of R_{2500} . As a consequence if the radius is not properly measured, due for instance

to erroneous estimations of the density contrast, the estimation of the depletion will be biased. Our purpose in this study being to constrain the hydrostatic mass bias and its evolution, we need a robust prior on the depletion factor, due to the degeneracy between Υ and B . A bias in the value of the depletion due to an incorrectly measured radius would then impact our results on the mean value and evolution of B .

5.3. Discussing the tension on the bias value

Finally, we highlight that the value of $B_0 = 0.779 \pm 0.089$ we found for the full sample is in agreement with a collection of other studies including the aforementioned weak-lensing and X-ray studies, and with works from hydrodynamical simulations, as we show in Figure 11. The works shown in Figure 11 are those for which the bias is known at R_{500} with a central value and error bars, where the mean mass and redshift of the samples are available. We show however that this value is incompatible with the values $B_0 = 0.62 \pm 0.03$ from Planck Collaboration et al. (2020), or $B_0 \lesssim 0.67$ from Salvati et al. (2018), needed to reconcile local measurements of the bias with the combination of CMB and tSZ number counts measurements. Indeed we show in Figure 11, that the tension is alleviated only for the highest redshifts, and more particularly for the highest masses, for clusters with $M \gtrsim 10^{15} M_\odot$.

Similarly the X-COP study (Eckert et al. 2019) shows that assuming a bias $B = 0.58 \pm 0.04$ from Planck Collaboration et al. (2016) results in gas fractions which are way lower than expected, as they find a median gas fraction of their sample $f_{\text{gas}, B=0.58} = 0.108 \pm 0.006$. This would imply that the galaxy clusters from their sample are missing about a third of their gas. A low value of the bias thus seems highly unlikely seeing its implications on the gas content of galaxy clusters.

We show a similar result in this work. Indeed, from equation 6, it is possible to compute the expected universal baryon fraction for a certain value of the bias :

$$\frac{\Omega_b}{\Omega_m} = (f_{\text{gas}} + f_*) \frac{1}{KA(z)} \frac{B(M, z)}{\Upsilon(M, z)} \left(\frac{D_A(z)}{D_A(z)^{\text{ref}}} \right)^{3/2}, \quad (17)$$

meaning $\Omega_b/\Omega_m \propto B$. When assuming a low value of the bias $B = 0.62 \pm 0.03$ from Planck Collaboration et al. (2020), we show that the derived baryon fraction becomes $\Omega_b/\Omega_m = 0.124 \pm 0.015$, which is incompatible with the value of the baryon fraction derived from the CMB, $\Omega_b/\Omega_m = 0.156 \pm 0.003$ (Planck Collaboration et al. 2020), as we show in Figure 12. Assuming a low value of the bias would then imply that the universe hosts roughly 20% less baryons than expected. We thus argue that a value of the bias $B = 0.62 \pm 0.03$ seems highly unlikely provided our gas fraction data.

6. Conclusion

We measured the gas mass fraction of galaxy clusters at R_{500} , and used it to constrain a possible mass and redshift evolution of the hydrostatic mass bias. To do so, we compared the cosmological constraints we obtained when assuming a varying bias to those we obtained when assuming a constant B . We show that assuming a redshift evolution seems necessary when performing a cosmological analysis using f_{gas} data at R_{500} . Indeed we show a significant degeneracy between the redshift dependence of the bias β and the matter density Ω_m . This degeneracy implies that high and close to zero β push the matter density to higher values. As a consequence, assuming a constant bias implies $\Omega_m > 0.849$,

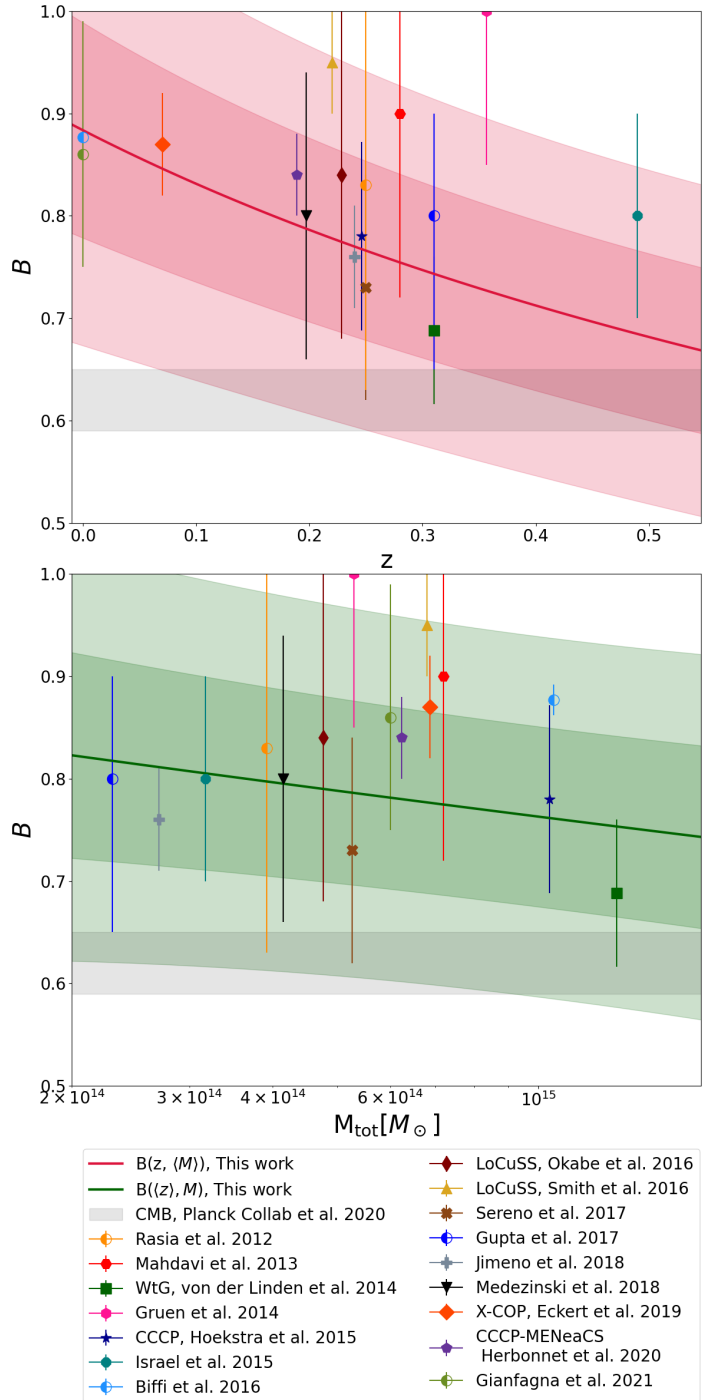


Fig. 11. Comparison of our value of the mass bias depending on mass and redshift with other X-ray, weak lensing and hydrodynamical simulation works. In both panels, the shaded areas mark the 1 and 2 σ confidence levels and the grey band marks the value preferred by CMB observations of $B = 0.62 \pm 0.03$. The half-filled circles are hydrodynamical simulation works, other points are works from observations.

Top : Value of the bias depending on redshift, which we computed at the mean mass of our sample.

Bottom : Value of the bias depending on mass, which we computed at the mean redshift of our sample.

References : Rasia et al. (2012), Mahdavi et al. (2013), von der Linden et al. (2014), Gruen et al. (2014), Hoekstra et al. (2015), Israel et al. (2015), Biffi et al. (2016), Okabe & Smith (2016), Smith et al. (2016), Sereno et al. (2017), Gupta et al. (2017), Jimeno et al. (2018), Medezinski et al. (2018), Eckert et al. (2019), Salvati et al. (2019), Herbonnet et al. (2020), Planck Collaboration et al. (2020), Gianfagna et al. (2021)

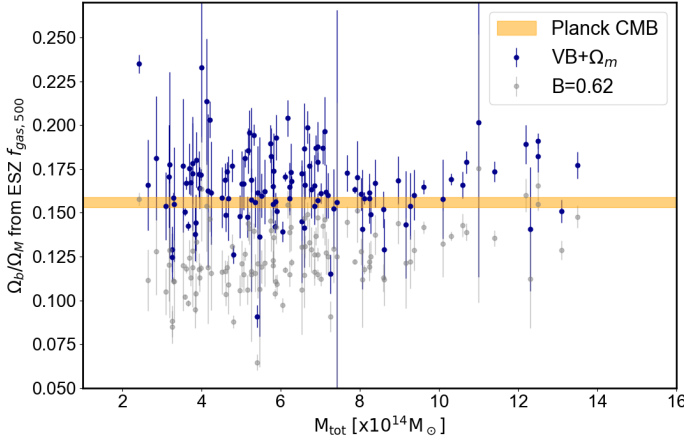


Fig. 12. Comparison of the expected baryon fraction Ω_b/Ω_m between the bias we derived in the $\text{VB} + \Omega_m$ scenario and $B = 0.62$ from (Planck Collaboration et al. 2020).

which is aberrant. Forcing Ω_m to have sensible values by imposing a Planck Collaboration et al. (2020) prior in turns induces $\beta = -0.64 \pm 0.17$, in a 3.8σ tension with 0.

We show however that these results are strongly dependent on the considered sample. Indeed for the least massive clusters of our sample at the lowest redshifts, we show an important decreasing trend of B with redshift and no trend with mass, with the set $(\alpha, \beta) = (0.08 \pm 0.10, -1.14^{+0.33}_{-0.73})$. On the other hand, for the most massive clusters at highest redshifts we observe no variation with redshift but are favoring a decreasing evolution with mass, with $(\alpha, \beta) = (-0.150 \pm 0.061, -0.14 \pm 0.23)$. When we consider the full sample, the results we obtain are lying in between the two extremes, largely favouring a decreasing trend of B with redshift yet remaining compatible with no mass trend of the bias as we obtain $(\alpha, \beta) = (-0.47 \pm 0.037, -0.64 \pm 0.17)$. We remind however that other selection effects might affect our results as the cluster at the highest redshifts are also generally the most massive.

In order to identify and rule out different sources of systematic effects in our study, we looked at the possibility of being subject to instrumental calibration effects. Using mass measurements of the galaxy clusters in our sample both from *Chandra* and *XMM-Newton*, we find no evidence of a bias which would significantly change our results. In this study we assumed a power-law description for the evolution of the bias. We look at the effect of this choice of parametrization by comparing our results to those we obtain when assuming a linear evolution of B with redshift. We find no major difference with the power-law case, as we still observe a strong degeneracy between the redshift evolution of B and Ω_m , favoring an evolution of the bias with redshift when considering a Planck prior on Ω_m . Furthermore the sample dependence we observe for the power-law case holds true when assuming a linear evolution of the bias.

Despite these results, we stress that we remain compatible with a collection of X-ray, weak lensing, and hydrodynamical simulation works regarding the mean value of the bias, as we find $B = 0.779 \pm 0.089$. This value remains on the other hand in tension with the value required from the combination CMB observations and tSZ cluster counts to alleviate the tension on σ_8 .

Finally, we remind that this work focused on gas fractions taken at R_{500} , and tried to obtain constraints on two cosmological parameters, the universal baryon fraction Ω_b/Ω_m and the matter

density of the universe Ω_m , which are the two parameters mainly probed by f_{gas} . We thus argue that the gas fraction can be used to put constraints on the cosmological model, albeit provided that one properly models the gas effects taking place inside clusters, and provided that f_{gas} is used in combination with other probes.

Acknowledgements. The authors acknowledge the fruitful discussions and comments from Hideki Tanimura, Daniela Galárraga-Espinosa, Edouard Lecoq, Joseph Kuruviña and Celine Gouin. The authors also thank the organisers and participants of the 2021 edition of the "Observing the mm Universe with the NIKA2 Camera" conference for their useful comments and discussions. RW acknowledges financial support from the from the Ecole Doctorale d'Astronomie et d'Astrophysique d'Ile-de-France (ED AAIF). This research has made use of the SZ-Cluster Database operated by the Integrated Data and Operation Center (IDOC) at the Institut d'Astrophysique Spatiale (IAS) under contract with CNES and CNRS. This project was carried out using the Python libraries matplotlib (Hunter 2007), numpy (Harris et al. 2020), astropy (Astropy Collaboration et al. 2013), Astropy Collaboration et al. (2018) and pandas (Reback et al. 2021). It also made use of the Python library for MCMC sampling emcee (Foreman-Mackey et al. 2013), and of the getdist (Lewis 2019) package to read posterior distributions.

References

Allen, S. W., Evrard, A. E., & Mantz, A. B. 2011, ARA&A, 49, 409
 Allen, S. W., Rapetti, D. A., Schmidt, R. W., et al. 2008, MNRAS, 383, 879
 Allen, S. W., Schmidt, R. W., & Fabian, A. C. 2002, MNRAS, 334, L11
 Andrade-Santos, F., Pratt, G. W., Melin, J.-B., et al. 2021, ApJ, 914, 58
 Astropy Collaboration, Price-Whelan, A. M., Sipőcz, B. M., et al. 2018, AJ, 156, 123
 Astropy Collaboration, Robitaille, T. P., Tollerud, E. J., et al. 2013, A&A, 558, A33
 Balmès, I., Rasera, Y., Corasaniti, P.-S., & Alimi, J.-M. 2013, Monthly Notices of the Royal Astronomical Society, 437, 2328
 Battaglia, N., Bond, J. R., Pfrommer, C., & Sievers, J. L. 2012, ApJ, 758, 74
 Battaglia, N., Bond, J. R., Pfrommer, C., & Sievers, J. L. 2013, ApJ, 777, 123
 Bennett, J. S. & Sijacki, D. 2021, arXiv e-prints, arXiv:2110.07326
 Biffi, V., Borgani, S., Murante, G., et al. 2016, ApJ, 827, 112
 Borgani, S. & Kravtsov, A. 2011, Advanced Science Letters, 4, 204
 Crain, R. A., Eke, V. R., Frenk, C. S., et al. 2007, MNRAS, 377, 41
 Cui, W., Knebe, A., Yepes, G., et al. 2018, MNRAS, 480, 2898
 Eckert, D., Ghirardini, V., Ettori, S., et al. 2019, A&A, 621, A40
 Eke, V. R., Navarro, J. F., & Frenk, C. S. 1998, ApJ, 503, 569
 Foreman-Mackey, D., Hogg, D. W., Lang, D., & Goodman, J. 2013, PASP, 125, 306
 Galárraga-Espinosa, D., Langer, M., & Aghanim, N. 2021, arXiv e-prints, arXiv:2109.06198
 Gianfagna, G., De Petris, M., Yepes, G., et al. 2021, MNRAS, 502, 5115
 Gruen, D., Seitz, S., Brimiouille, F., et al. 2014, MNRAS, 442, 1507
 Gupta, N., Saro, A., Mohr, J. J., Dolag, K., & Liu, J. 2017, MNRAS, 469, 3069
 Harris, C. R., Millman, K. J., van der Walt, S. J., et al. 2020, Nature, 585, 357
 Henden, N. A., Puchwein, E., & Sijacki, D. 2020, MNRAS, 498, 2114
 Herbonnet, R., Sifón, C., Hoekstra, H., et al. 2020, MNRAS, 497, 4684
 Hoekstra, H., Herbonnet, R., Muzzin, A., et al. 2015, MNRAS, 449, 685
 Hoekstra, H., Mahdavi, A., Babul, A., & Bildfell, C. 2012, MNRAS, 427, 1298
 Holanda, R. F. L., Pordeus-da-Silva, G., & Pereira, S. H. 2020, J. Cosmology Astropart. Phys., 2020, 053
 Hunter, J. D. 2007, Computing in Science and Engineering, 9, 90
 Israel, H., Schellenberger, G., Nevalainen, J., Massey, R., & Reiprich, T. H. 2015, MNRAS, 448, 814
 Jimeno, P., Diego, J. M., Broadhurst, T., De Martino, I., & Lazkoz, R. 2018, MNRAS, 478, 638
 Kravtsov, A. V. & Borgani, S. 2012, ARA&A, 50, 353
 Kravtsov, A. V., Nagai, D., & Vikhlinin, A. A. 2005, ApJ, 625, 588
 Lau, E. T., Kravtsov, A. V., & Nagai, D. 2009, ApJ, 705, 1129
 Lewis, A. 2019, arXiv e-prints, arXiv:1910.13970
 Lovisari, L., Schellenberger, G., Sereno, M., et al. 2020, ApJ, 892, 102
 Mahdavi, A., Hoekstra, H., Babul, A., et al. 2013, ApJ, 767, 116
 Mantz, A. B., Allen, S. W., Morris, R. G., et al. 2014, MNRAS, 440, 2077
 Mantz, A. B., Morris, R. G., Allen, S. W., et al. 2022, MNRAS, 510, 131
 Maurogordato, S., Cappi, A., Ferrari, C., et al. 2008, A&A, 481, 593
 McCarthy, I. G., Babul, A., Holder, G. P., & Balogh, M. L. 2003a, ApJ, 591, 515
 McCarthy, I. G., Holder, G. P., Babul, A., & Balogh, M. L. 2003b, ApJ, 591, 526
 McCarthy, I. G., Schaye, J., Bird, S., & Le Brun, A. M. C. 2017, MNRAS, 465, 2936
 Medezinski, E., Battaglia, N., Umetsu, K., et al. 2018, PASJ, 70, S28
 Nelson, K., Lau, E. T., & Nagai, D. 2014, ApJ, 792, 25

Okabe, N. & Smith, G. P. 2016, MNRAS, 461, 3794

Planck Collaboration, Ade, P. A. R., Aghanim, N., et al. 2014, A&A, 571, A20

Planck Collaboration, Ade, P. A. R., Aghanim, N., et al. 2011, A&A, 536, A8

Planck Collaboration, Ade, P. A. R., Aghanim, N., et al. 2016, A&A, 594, A24

Planck Collaboration, Aghanim, N., Akrami, Y., et al. 2020, A&A, 641, A6

Planelles, S., Borgani, S., Dolag, K., et al. 2013, MNRAS, 431, 1487

Poole, G. B., Babul, A., McCarthy, I. G., et al. 2007, MNRAS, 380, 437

Pratt, G. W., Arnaud, M., Biviano, A., et al. 2019, Space Sci. Rev., 215, 25

Rasia, E., Ettori, S., Moscardini, L., et al. 2006, MNRAS, 369, 2013

Rasia, E., Meneghetti, M., Martino, R., et al. 2012, New Journal of Physics, 14, 055018

Reback, J., McKinney, W., jbrockmendel, et al. 2021, pandas-dev/pandas: Pandas 1.2.4

Ruan, J. J., Quinn, T. R., & Babul, A. 2013, MNRAS, 432, 3508

Sakr, Z., Ilić, S., Blanchard, A., Bittar, J., & Farah, W. 2018, A&A, 620, A78

Salvati, L., Douspis, M., & Aghanim, N. 2018, A&A, 614, A13

Salvati, L., Douspis, M., Ritz, A., Aghanim, N., & Babul, A. 2019, A&A, 626, A27

Sarazin, C. L. 1988, X-ray emission from clusters of galaxies

Schellenberger, G., Reiprich, T. H., Lovisari, L., Nevalainen, J., & David, L. 2015, A&A, 575, A30

Sembolini, F., Yepes, G., Pearce, F. R., et al. 2016, MNRAS, 457, 4063

Sereno, M., Covone, G., Izzo, L., et al. 2017, MNRAS, 472, 1946

Sereno, M. & Ettori, S. 2017, MNRAS, 468, 3322

Shi, X., Komatsu, E., Nelson, K., & Nagai, D. 2015, MNRAS, 448, 1020

Smith, G. P., Mazzotta, P., Okabe, N., et al. 2016, MNRAS, 456, L74

Sunyaev, R. A. & Zeldovich, Y. B. 1972, Comments on Astrophysics and Space Physics, 4, 173

Vazza, F., Brunetti, G., Kritsuk, A., et al. 2009, A&A, 504, 33

von der Linden, A., Mantz, A., Allen, S. W., et al. 2014, MNRAS, 443, 1973

White, S. D. M., Navarro, J. F., Evrard, A. E., & Frenk, C. S. 1993, Nature, 366, 429

Wicker, R., Douspis, M., Salvati, L., & Aghanim, N. 2022, in European Physical Journal Web of Conferences, Vol. 257, European Physical Journal Web of Conferences, 00046

Appendix A: Cluster sample

The redshifts, gas masses, total masses, and gas mass fractions inside R_{500} of the clusters we used for this study are given in Table A.1. The redshifts and gas and total masses for the clusters were taken from [Lovisari et al. \(2020\)](#). We computed the gas fractions from these masses.

Table A.1. The 120 clusters we used in this study, from the *Planck*-ESZ sample. Columns: (1) Name in the ESZ catalog; (2) Cluster redshift; (3) Gas mass; (4) Total mass derived assuming hydrostatic equilibrium; (5) Gas mass fraction.

Planck Name	z	$M_{\text{gas},500} [\times 10^{14} M_{\odot}]$	$M_{\text{tot},500} [\times 10^{14} M_{\odot}]$	f_{gas}
G000.44-41.83	0.165	0.661 ± 0.036	5.01 ± 0.55	0.132 ± 0.016
G002.74-56.18	0.141	0.563 ± 0.021	4.96 ± 0.43	0.114 ± 0.011
G003.90-59.41	0.151	0.865 ± 0.008	6.94 ± 0.19	0.125 ± 0.004
G006.70-35.54	0.089	0.427 ± 0.008	2.42 ± 0.04	0.176 ± 0.004
G006.78+30.46	0.203	3.200 ± 0.020	17.50 ± 0.20	0.183 ± 0.002
G008.44-56.35	0.149	0.464 ± 0.005	3.61 ± 0.08	0.129 ± 0.003
G008.93-81.23	0.307	1.560 ± 0.010	10.30 ± 0.20	0.151 ± 0.003
G021.09+33.25	0.151	1.040 ± 0.030	6.88 ± 0.20	0.151 ± 0.006
G036.72+14.92	0.152	0.816 ± 0.029	5.21 ± 0.32	0.157 ± 0.011
G039.85-39.98	0.176	0.532 ± 0.036	3.77 ± 0.47	0.141 ± 0.020
G042.82+56.61	0.072	0.601 ± 0.008	4.65 ± 0.15	0.129 ± 0.005
G046.08+27.18	0.389	0.990 ± 0.035	6.26 ± 0.61	0.158 ± 0.016
G046.50-49.43	0.085	0.624 ± 0.009	6.05 ± 0.28	0.103 ± 0.005
G049.20+30.86	0.164	0.651 ± 0.007	5.86 ± 0.16	0.111 ± 0.003
G049.33+44.38	0.097	0.385 ± 0.018	3.84 ± 0.46	0.100 ± 0.013
G049.66-49.50	0.098	0.441 ± 0.008	4.81 ± 0.21	0.092 ± 0.004
G053.52+59.54	0.113	0.703 ± 0.010	5.87 ± 0.20	0.120 ± 0.004
G055.60+31.86	0.224	0.941 ± 0.012	6.54 ± 0.18	0.144 ± 0.004
G055.97-34.88	0.124	0.344 ± 0.009	5.41 ± 0.45	0.064 ± 0.006
G056.81+36.31	0.095	0.512 ± 0.004	3.98 ± 0.08	0.129 ± 0.003
G056.96-55.07	0.447	1.520 ± 0.010	9.62 ± 0.25	0.158 ± 0.004
G057.26-45.35	0.397	1.860 ± 0.020	13.10 ± 0.60	0.142 ± 0.007
G058.28+18.59	0.065	0.454 ± 0.020	3.72 ± 0.07	0.122 ± 0.003
G062.42-46.41	0.091	0.287 ± 0.013	3.26 ± 0.39	0.088 ± 0.011
G067.23+67.46	0.171	1.040 ± 0.010	8.11 ± 0.18	0.128 ± 0.003
G071.61+29.79	0.157	0.532 ± 0.051	4.24 ± 0.76	0.125 ± 0.026
G072.63+41.46	0.228	1.650 ± 0.020	10.70 ± 0.40	0.154 ± 0.006
G072.80-18.72	0.143	0.825 ± 0.011	5.33 ± 0.17	0.155 ± 0.005
G073.96-27.82	0.233	1.710 ± 0.020	11.40 ± 0.40	0.150 ± 0.006
G080.38-33.20	0.107	0.383 ± 0.003	3.66 ± 0.07	0.105 ± 0.002
G080.99-50.90	0.3	0.955 ± 0.020	6.62 ± 0.32	0.144 ± 0.008
G083.28-31.03	0.412	1.240 ± 0.030	7.68 ± 0.47	0.161 ± 0.011
G085.99+26.71	0.179	0.397 ± 0.047	3.31 ± 0.68	0.120 ± 0.028
G086.45+15.29	0.26	0.930 ± 0.021	5.74 ± 0.33	0.162 ± 0.010
G092.73+73.46	0.228	1.070 ± 0.020	6.18 ± 0.32	0.173 ± 0.010
G093.91+34.90	0.081	0.549 ± 0.044	4.68 ± 0.71	0.117 ± 0.020
G096.87+24.21	0.3	0.628 ± 0.108	5.47 ± 2.40	0.115 ± 0.054
G097.73+38.11	0.171	0.687 ± 0.017	4.21 ± 0.21	0.163 ± 0.009
G098.95+24.86	0.093	0.299 ± 0.014	3.25 ± 0.35	0.092 ± 0.011
G106.73-83.22	0.292	0.831 ± 0.026	5.18 ± 0.36	0.160 ± 0.012
G107.11+65.31	0.292	0.694 ± 0.030	7.26 ± 0.75	0.096 ± 0.011
G113.82+44.35	0.225	0.570 ± 0.028	3.87 ± 0.32	0.147 ± 0.014
G124.21-36.48	0.197	0.781 ± 0.033	5.81 ± 0.62	0.134 ± 0.015
G125.70+53.85	0.302	0.964 ± 0.043	6.78 ± 0.69	0.142 ± 0.016
G139.19+56.35	0.322	1.020 ± 0.140	7.42 ± 5.68	0.137 ± 0.107
G149.73+34.69	0.182	1.160 ± 0.050	7.12 ± 0.71	0.163 ± 0.018
G157.43+30.33	0.45	0.964 ± 0.035	6.23 ± 0.52	0.155 ± 0.014
G159.85-73.47	0.206	0.988 ± 0.047	6.73 ± 0.70	0.147 ± 0.017
G164.18-38.89	0.074	0.630 ± 0.028	5.07 ± 0.45	0.124 ± 0.012
G166.13+43.39	0.217	0.868 ± 0.022	6.86 ± 0.48	0.127 ± 0.009
G167.65+17.64	0.174	0.925 ± 0.026	5.88 ± 0.40	0.157 ± 0.012
G171.94-40.65	0.27	1.500 ± 0.090	12.30 ± 3.40	0.122 ± 0.034
G180.24+21.04	0.546	2.340 ± 0.050	12.50 ± 0.60	0.187 ± 0.010
G182.44-28.29	0.088	0.958 ± 0.020	6.93 ± 0.18	0.138 ± 0.005
G182.63+55.82	0.206	0.688 ± 0.015	4.77 ± 0.26	0.144 ± 0.008
G186.39+37.25	0.282	1.240 ± 0.060	9.28 ± 1.19	0.134 ± 0.018
G195.62+44.05	0.295	0.877 ± 0.049	5.82 ± 0.72	0.151 ± 0.020
G195.77-24.30	0.203	1.110 ± 0.020	6.67 ± 0.32	0.166 ± 0.009
G218.85+35.50	0.175	0.430 ± 0.020	3.86 ± 0.45	0.111 ± 0.014
G225.92-19.99	0.46	2.190 ± 0.540	11.00 ± 4.40	0.199 ± 0.094

Table A.1 continued from previous page

Planck Name	z	$M_{gas} [\times 10^{14} M_{\odot}]$	$M_{tot} [\times 10^{14} M_{\odot}]$	f_{gas}
G226.17-21.91	0.099	0.510 ± 0.011	4.61 ± 0.32	0.111 ± 0.008
G226.24+76.76	0.143	0.834 ± 0.006	6.28 ± 0.12	0.133 ± 0.003
G228.15+75.19	0.545	1.350 ± 0.070	7.94 ± 0.96	0.170 ± 0.022
G228.49+53.12	0.143	0.587 ± 0.021	5.16 ± 0.42	0.114 ± 0.010
G229.21-17.24	0.171	0.656 ± 0.084	5.26 ± 1.84	0.125 ± 0.046
G229.94+15.29	0.07	0.851 ± 0.013	7.01 ± 0.26	0.121 ± 0.005
G236.95-26.67	0.148	0.696 ± 0.014	5.91 ± 0.33	0.118 ± 0.007
G241.74-30.88	0.271	0.759 ± 0.025	5.80 ± 0.42	0.131 ± 0.010
G241.77-24.00	0.139	0.395 ± 0.004	3.29 ± 0.06	0.120 ± 0.003
G241.97+14.85	0.169	0.710 ± 0.069	4.13 ± 0.64	0.172 ± 0.031
G244.34-32.13	0.284	1.140 ± 0.030	6.94 ± 0.54	0.164 ± 0.013
G244.69+32.49	0.153	0.504 ± 0.017	3.70 ± 0.31	0.136 ± 0.012
G247.17-23.32	0.152	0.416 ± 0.037	3.17 ± 0.54	0.131 ± 0.025
G249.87-39.86	0.165	0.402 ± 0.036	2.86 ± 0.56	0.141 ± 0.030
G250.90-36.25	0.2	0.674 ± 0.027	5.36 ± 0.51	0.126 ± 0.013
G252.96-56.05	0.075	0.390 ± 0.003	3.58 ± 0.05	0.109 ± 0.001
G253.47-33.72	0.191	0.571 ± 0.033	4.52 ± 0.48	0.126 ± 0.015
G256.45-65.71	0.22	0.718 ± 0.057	5.42 ± 0.89	0.132 ± 0.024
G257.34-22.18	0.203	0.451 ± 0.082	3.19 ± 0.88	0.141 ± 0.047
G260.03-63.44	0.284	1.000 ± 0.030	7.15 ± 0.73	0.140 ± 0.015
G262.25-35.36	0.295	1.080 ± 0.070	6.59 ± 0.90	0.164 ± 0.025
G262.71-40.91	0.42	1.220 ± 0.070	9.16 ± 2.11	0.133 ± 0.032
G263.16-23.41	0.227	1.120 ± 0.020	7.07 ± 0.35	0.158 ± 0.008
G263.66-22.53	0.164	1.050 ± 0.020	8.59 ± 0.65	0.122 ± 0.010
G266.03-21.25	0.296	2.170 ± 0.020	12.50 ± 0.30	0.174 ± 0.004
G269.31-49.87	0.085	0.319 ± 0.026	2.65 ± 0.41	0.120 ± 0.021
G271.19-30.96	0.37	1.280 ± 0.050	8.38 ± 0.68	0.153 ± 0.014
G271.50-56.55	0.3	0.979 ± 0.075	8.07 ± 2.11	0.121 ± 0.033
G272.10-40.15	0.059	0.779 ± 0.005	6.11 ± 0.09	0.127 ± 0.002
G277.75-51.73	0.44	1.440 ± 0.050	8.96 ± 0.73	0.161 ± 0.014
G278.60+39.17	0.307	1.330 ± 0.050	9.37 ± 0.87	0.142 ± 0.014
G280.19+47.81	0.156	0.744 ± 0.061	6.53 ± 1.70	0.114 ± 0.031
G282.49+65.17	0.077	0.664 ± 0.011	5.25 ± 0.22	0.126 ± 0.006
G283.16-22.93	0.45	1.050 ± 0.060	7.34 ± 1.14	0.143 ± 0.024
G284.46+52.43	0.441	1.690 ± 0.030	10.60 ± 0.50	0.159 ± 0.008
G284.99-23.70	0.39	1.480 ± 0.080	10.10 ± 1.50	0.147 ± 0.023
G285.63-17.24	0.35	0.820 ± 0.078	6.59 ± 1.00	0.124 ± 0.022
G286.58-31.25	0.21	0.718 ± 0.024	5.52 ± 0.45	0.130 ± 0.011
G286.99+32.91	0.39	2.200 ± 0.060	12.20 ± 0.70	0.180 ± 0.011
G288.61-37.65	0.127	0.735 ± 0.067	4.00 ± 0.70	0.184 ± 0.036
G292.51+21.98	0.3	1.130 ± 0.020	8.03 ± 0.49	0.141 ± 0.009
G294.66-37.02	0.274	0.988 ± 0.036	7.20 ± 0.59	0.137 ± 0.012
G304.67-31.66	0.193	0.538 ± 0.076	4.16 ± 1.10	0.129 ± 0.039
G304.84-41.42	0.41	1.140 ± 0.030	8.28 ± 0.64	0.138 ± 0.011
G306.68+61.06	0.085	0.503 ± 0.017	3.93 ± 0.31	0.128 ± 0.011
G306.80+58.60	0.085	0.582 ± 0.014	4.60 ± 0.26	0.127 ± 0.008
G308.32-20.23	0.48	1.050 ± 0.050	8.61 ± 1.22	0.122 ± 0.018
G313.36+61.11	0.183	1.050 ± 0.000	7.87 ± 0.10	0.133 ± 0.002
G313.87-17.10	0.153	1.070 ± 0.010	8.24 ± 0.25	0.130 ± 0.004
G318.13-29.57	0.217	0.743 ± 0.040	5.59 ± 0.64	0.133 ± 0.017
G321.96-47.97	0.094	0.483 ± 0.017	3.95 ± 0.29	0.122 ± 0.010
G324.49-44.97	0.095	0.347 ± 0.020	3.09 ± 0.40	0.112 ± 0.016
G332.23-46.36	0.098	0.706 ± 0.008	5.09 ± 0.15	0.139 ± 0.004
G332.88-19.28	0.147	0.774 ± 0.021	6.22 ± 0.38	0.124 ± 0.008
G335.59-46.46	0.076	0.461 ± 0.054	3.53 ± 0.74	0.131 ± 0.031
G336.59-55.44	0.097	0.488 ± 0.046	3.78 ± 0.71	0.129 ± 0.027
G337.09-25.97	0.26	0.894 ± 0.034	5.75 ± 0.50	0.155 ± 0.015
G342.31-34.90	0.232	0.949 ± 0.045	6.85 ± 0.74	0.139 ± 0.016
G347.18-27.35	0.237	1.100 ± 0.050	8.24 ± 0.73	0.133 ± 0.013
G349.46-59.94	0.347	2.230 ± 0.040	13.50 ± 0.60	0.165 ± 0.008